



Pyridine N-induced intra-pore and interfacial dual-confined Pd⁰-Pd^{δ+} synergistic catalysis for ultra-stable dehydrogenation of dodecahydro-N-propylcarbazole

Li Liu^a, Qingyang Zhang^a, Chengwei Deng^{b,*}, Chenggen Li^c, Yinheng Zhao^a, Rongyi Gao^a, Ting Zhu^a, Yuan Dong^a, Hansong Cheng^a, Ming Yang^{a,c,**}

^a Hubei Hydrogen Energy Technology Innovation Center, Faculty of Materials Science and Chemistry, China University of Geosciences, Wuhan 430074, PR China

^b State Key Laboratory of Space Power-Sources Technology, Shanghai Institute of Space Power Sources, Shanghai 200245, PR China

^c Key Laboratory of Geological Survey and Evaluation of Ministry of Education, Institute of Advanced Studies, China University of Geosciences, Wuhan 430074, PR China

ARTICLE INFO

Keywords:

Carbon-Nitrogen layer
Dual-confinement catalysis
Pd⁰-Pd^{δ+} synergistic effect
Ultra-stable dehydrogenation
Liquid Organic Hydrogen Carriers

ABSTRACT

We developed nano Pd catalysts, encapsulated within carbon-nitrogen layers at both intra-pore and interfacial levels on SiO₂, via in-situ thermolysis of metal-organic coordination compounds. The catalysts dehydrogenation efficacy is greatly influenced by thermolysis temperature and ligand-to-metal ratio. The Pd-C-N₂/SiO₂-600 catalyst notably achieved complete dehydrogenation of 12 H-NPCZ within 240 minutes, demonstrating exceptional stability over 10 cycles without significant degradation, highlighting its viability for commercial use. Characterizations revealed that the C-N layer integration improves Pd nanoparticle dispersion and reduces strong acid site formation on catalyst surface. This synergy between the C-N layer and Pd nanoparticles promotes the formation and stabilization of Pd^{δ+} species, optimizing them as adsorption sites for dehydrogenation with appropriate acid strength. Moreover, this interaction adjusts the electronic states of Pd⁰ active sites, optimizing adsorption dynamics for intermediates. This cooperative action between Pd⁰ and Pd^{δ+} significantly boosts the desorption rate of dehydrogenation products, substantially improving the catalysis performance.

1. Introduction

Amid the escalating global energy crisis and the worsening environmental pollution, the development of innovative clean energy solutions has become a pivotal trend in the global energy landscape. Hydrogen, renowned for its zero pollution footprint and high efficiency as a renewable energy source, is viewed as a promising alternative to conventional fossil fuels.[1,2] Nonetheless, challenges related to hydrogen storage and transportation remain significant obstacles to its broad adoption.[3,4] Liquid Organic Hydrogen Carrier (LOHC) technology, utilizing unsaturated aromatic hydrocarbons for hydrogen storage and enabling hydrogen release through reversible catalytic hydrogenation and dehydrogenation cycles [5,6], stands out as one of the most promising solutions among various hydrogen storage strategies. Heterocyclic aromatics, such as carbazole family, are widely used as

hydrogen carriers within LOHC systems due to their high hydrogen storage capacity and favorable dehydrogenation conditions, attracting significant research interest. [7–9]

The efficacy of dehydrogenation catalysts is crucial for leveraging N-heterocyclic aromatic hydrogen storage materials. Palladium (Pd), with its distinctive electronic structure, demonstrates exceptional effectiveness in catalyzing the dehydrogenation of N-heterocycles.[10,11] However, the scarcity and substantial cost of Pd limit its scalability for widespread applications. A key challenge involves reducing the Pd loading while maximizing the efficiency of Pd atom utilization in dehydrogenation catalysts, essential for the expansion of liquid organic hydrogen storage technology.

An effective strategy to enhance the utilization efficiency of precious Pd atoms involves minimizing the size of metal nanoparticles to expose highly active sites. [12–14] Ding et al. [15] successfully encapsulated Pd

* Corresponding author.

** Corresponding author at: Hubei Hydrogen Energy Technology Innovation Center, Faculty of Materials Science and Chemistry, China University of Geosciences, Wuhan 430074, PR China.

E-mail addresses: dengchengwei@spacechina.com (C. Deng), yangming8180@gmail.com (M. Yang).

<https://doi.org/10.1016/j.apcatb.2024.123987>

Received 21 February 2024; Received in revised form 14 March 2024; Accepted 19 March 2024

Available online 20 March 2024

0926-3373/© 2024 Elsevier B.V. All rights reserved.

nanoparticles within the MIL-101 pore channels, producing nanoparticles with a 3 nm diameter. These nanoparticles can achieve complete dehydrogenation of dodecahydro-N-propylcarbazole (12 H-NPCZ) within 240 minutes and exhibit reusability for up to five cycles. Dong et al. [16] suggested that the dehydrogenation activity of Pd nanoparticles depends not only on their size but also on their structural configuration. Characterizations of Pd nanoparticles supported on nanodiamonds showed that when the average coordination number of palladium species reaches 4.4, atomic layer palladium clusters are fully exposed, optimizing the catalytic performance for the activation and desorption of dehydrogenation products from dodecahydro-N-ethylcarbazole (12 H-NECZ). Ma et al. synthesized noble metal clusters fully exposed on defect-rich graphene. By adjusting the coordination number of metal clusters, the atomically dispersed catalysts for dehydrogenation were obtained. These catalysts effectively modulate the adsorption and desorption of reaction intermediates, thereby enabling efficient activation of C-H bonds. Compared to nano-cluster catalysts, the atomically dispersed catalysts demonstrated significantly higher activity and selectivity. [17,18]

Nevertheless, the size and structure of Pd nanoparticles are not the only factors influencing dehydrogenation performance. Feng et al. [19] explored the dehydrogenation activity of 12 H-NECZ over Pd-based catalysts supported on C, TiO₂, and Al₂O₃, revealing that despite the size hierarchy of Pd particles being Pd/TiO₂ < Pd/C < Pd/Al₂O₃, their catalytic activity followed the sequence Pd/C > Pd/Al₂O₃ > Pd/TiO₂, indicating an association with the intrinsic properties of the supports. Further, Chen et al. [20] found that the dehydrogenation activity of 12 H-NPCZ correlates with the carrier's specific surface area and acid-base properties. Elevated specific surface areas and milder acidity levels of the carrier enhance the dispersion and stability of Pd nanoparticles, thereby augmenting the catalyst's dehydrogenation activity towards 12 H-NPCZ. These findings collectively indicate that the catalytic dehydrogenation efficiency of Pd-based catalysts is determined by an amalgam of factors, including Pd nanoparticle size, structural morphology, and the acid-base characteristics of the support.

Carbon-nitrogen (C-N) catalysis materials, characterized by their distinctive structural morphology and properties, have become a significant focus of research in recent years. [21,22] The subtle interaction between carbon and metals in these C-N materials not only enhances the catalyst's resistance to carbon buildup but also substantially improves the reducibility of the metallic substrate. Nitrogen acts as a stabilizing agent within C-N materials, effectively immobilizing metallic entities within a confined space and thus generating a notable confinement effect. The presence of diverse nitrogen configurations, including pyridinic, pyrrolic, triazine-based, graphitic, metal-coordinated, and tetra-coordinated N, equips the catalyst's surface with tunable acidity, basicity, and microelectronic properties, offering a tailored approach to catalytic activity. [23–25] This multifaceted role of nitrogen contributes to the dynamic and versatile nature of C-N catalytic materials, underscoring their potential in advancing catalytic performance through structural and electronic modulation.

Wei et al. [26] developed porous nitrogen-doped graphene layers encapsulating cobalt nanoparticles (CoO_x@CN) for the hydrogenation of quinoline, demonstrating enhanced catalytic activity and reusability compared to CoO_x nanoparticles positioned on the exterior surface of C-N. This improvement is credited to the encapsulated Co₃O₄ nanoparticles, which efficiently transition to metallic Co, thus facilitating hydrogen dissociation and augmenting catalytic performance. The encapsulation structure not only prevents the cobalt nanoparticles from aggregating and leaching but also mitigates the strong interaction between the N atom in the heterocycle and the active metal nanoparticles, improving the catalyst's cyclic stability. Beller et al. [27] synthesized a mixed phase of iron species and N-doped carbon for quinoline hydrogenation through the pyrolysis of Fe(OAc)₂ and N-phenyl-substituted pyridine. At 140 °C and 5 MPa H₂, they successfully generated 4 H-quinoline derivatives. Their findings highlight a crucial link

between the mixed-phase structure and the catalytic efficacy, although the mixed phase's composition is complex (including Fe₃C, metallic Fe, FeN_x, and CN_x), leaving the precise nature of the active site unclear. Moreover, Hu et al. [28] introduced a metal-free C-N catalyst that performs dehydrogenation of N-heterocycles at ambient temperature. Mechanistic investigations identify the active site as closely packed graphite nitrogen (CGNs), created during the carbonization of the precursor. While the CGN center can activate the C-H bond in N-heterocycles, dehydrogenation efficiency at room temperature remains modest, failing to achieve complete dehydrogenation. The stability and recyclability of dehydrogenation at elevated temperatures have not been confirmed. In summary, C-N materials play a pivotal role in catalysis through the confinement and modulation of the electronic structure at the active center. However, the potential for effectuating dehydrogenation, particularly in the context of LOHCs, is still an emerging area of research, signaling a promising but yet unexplored avenue for future investigations.

In this study, we adopted an in-situ pyrolysis approach using metal-organic ligands to synthesize C-N layer-encapsulated Pd nanoparticles on SiO₂ surfaces, introducing this method for the first time in the dehydrogenation reaction of 12 H-NPCZ. Our experimental findings reveal that the Pd-CN₂/SiO₂-600 catalyst achieves complete dehydrogenation of 12 H-NPCZ within 240 minutes, maintaining exceptional stability across 10 dehydrogenation cycles. This indicates its considerable potential for industrial applications. To understand the impact of C-N layer encapsulation on the morphology of Pd nanoparticles, comprehensive characterization studies were undertaken. Integrating dehydrogenation kinetics and density functional theory (DFT) calculations, we explored the dehydrogenation mechanism of 12 H-NPCZ. We elucidated how the encapsulation within a C-N layer enhances the dehydrogenation efficiency of Pd nanoparticles and discussed the correlation between the structural attributes of Pd nanoparticles and their catalytic dehydrogenation activity. These insights contribute significantly to the field, offering a valuable framework for the systematic design and industrial deployment of effective and durable LOHCs dehydrogenation catalysts.

2. Experimental

2.1. Catalyst synthesis

A solution was prepared by dissolving 0.0639 g of palladium acetate (0.2847 mmol) and a measured quantity of phenanthroline monohydrate in 15 ml of anhydrous ethanol. To this solution, 3 g of SiO₂ was added, and the mixture was stirred continuously for 4 hours before drying at 60 °C for 8 hours, yielding a pale-yellow precursor. This precursor underwent pyrolysis in a 10% H₂/Ar atmosphere for 4 hours at a specified temperature, increasing at a rate of 5 °C/min. Upon natural cooling to room temperature, the catalyst, designated as Pd-CN_x/SiO₂-Y, was obtained. Here, X denotes the molar ratio of phenanthroline to palladium acetate, and Y signifies the pyrolysis temperature, which was set at 500 °C, 600 °C, 700 °C, and 800 °C respectively. The preparation process of 20 g scale catalyst is shown in Figure S1.

Detailed preparation methods for SiO₂, the Pd/SiO₂-600 catalyst, and 12 H-NPCZ are provided in the Supporting Information.

2.2. Catalyst characterization

The pore structures of all materials were analyzed using an ASAP 2020 nitrogen adsorption instrument. Phase characterization of the samples was performed with X-ray diffraction (XRD) on a Bruker D8 instrument. Raman spectroscopy, conducted on a Witech alpha300R instrument, assessed the carbon layer structure within the catalyst. Inductively Coupled Plasma (ICP) analysis, performed on a PerkinElmer Optima 5300 DV instrument, determined the actual Pd content in the samples. CO pulse adsorption, H₂-Temperature Programmed Reduction

(H₂-TPR), H₂-Temperature Programmed Desorption (H₂-TPD), and NH₃-Temperature Programmed Desorption (NH₃-TPD) analyses were carried out on a Micromeritics AutoChem 2950II. X-ray Photoelectron Spectroscopy (XPS), conducted on an AVG Multilab 2000 spectrometer equipped with an Al target and C 1 s calibration, was used to analyze the surface elemental composition and atomic valence states. High-Resolution Transmission Electron Microscopy (HRTEM) characterized the surface morphology and elemental distribution of the catalyst. CO Diffuse Reflectance Infrared Fourier Transform (CO-DRIFT) spectroscopy was performed using a Bruker EQUINOX55 Fourier Transform Infrared Spectrometer.

2.3. DFT calculation model

This study explores the electron transfer between the active components of the catalyst and the carrier through Density Functional Theory (DFT) calculations, constructed using Materials Studio software and performed using the Vienna Ab-initio Simulation Package (VASP) on Linux. The core algorithm of VASP is based on DFT with periodic boundary conditions, utilizing the spin-polarized Generalized Gradient Approximation (GGA) with the Perdew-Burke-Ernzerhof (PBE) functional. Ultrasoft pseudopotentials described the ionic cores, with a plane-wave basis set cut-off energy of 400 eV. The Brillouin zone k-points were set at $1 \times 1 \times 1$ for constructing surface and adsorption models, with all calculations being spin-polarized to enhance the accuracy and realism of the simulations. The convergence criteria for structure and force were set at 1×10^{-5} eV/atom and 0.02 eV/Å, respectively.

To examine the electron transfer in Pd₆ clusters on C-N layers and SiO₂ surfaces, metal clusters adsorbed on nitrogen-doped carbon layers and SiO₂ surfaces were modeled using Material Studio software. The effect of nitrogen doping defects on Pd clusters was studied, with differential charge and Bader charge analyses further elucidating the catalyst's mechanism.

2.4. Catalytic dehydrogenation test

The catalyst's performance was assessed in an oil bath with magnetic

stirring. A mixture of 0.2 g of the catalyst, 1 g of 12 H-NPCZ, and 3 g of 1,3,5-trimethylbenzene was dehydrogenated in a round-bottom flask at 190 °C and 101 kPa. Periodic sampling during the reaction was conducted using a capillary tube, with an Agilent GC 7890B gas chromatograph analyzing the liquid composition to determine conversion rates.

The catalyst's cyclic stability was evaluated over 10 consecutive dehydrogenation experiments. Following each test, the catalyst was isolated, rinsed with ethanol, dried, and then re-evaluated under the original reaction conditions, repeating this process 10 times. The Hiden HAL 201 RC mass spectrometer (with a detection limit of less than 1 ppm) was used to assess the purity of the gas released during the dehydrogenation of 12 H-NPCZ catalyzed by Pd-CN₂/SiO₂-600.

3. Results and discussions

3.1. Catalyst structural characterization

The comparative analysis of the Raman spectra between Pd/SiO₂-600 and Pd-CN₂/SiO₂-600, illustrated in Figure S2, identifies pronounced peaks at 1380 cm⁻¹ and 1600 cm⁻¹ for Pd-CN₂/SiO₂-600. These peaks signify the development of abundant carbon species on the SiO₂ surface resultant from the pyrolysis of phenanthroline.[29] The morphological assessment of Pd/SiO₂-600 and Pd-CN₂/SiO₂-600, depicted in Fig. 1(a, b), uncovers the agglomerated clusters of Pd nanoparticles on Pd/SiO₂-600 with a predominant size range of 20–30 nm. Conversely, Pd-CN₂/SiO₂-600 is characterized by the presence of scant, finely dispersed Pd nanoparticles, primarily sized between 2 and 4 nm. The lattice fringe patterns of particles in Pd-CN₂/SiO₂-600, as shown in Fig. 1(c), where a lattice spacing of 0.225 nm corresponds to the Pd(111) facet, frequently acknowledged as the advantageous facet for the dehydrogenation of 12 H-NPCZ. [12,13] Fig. 1(d) illustrates the elemental dispersion on Pd-CN₂/SiO₂-600, showing a uniform distribution of Pd, C, and N elements across the SiO₂ carrier. The congruence in the distribution patterns of Pd and the C, N elements implies a tight integration between Pd and the C-N layer. Raman and TEM analyses of Pd-CN₂/SiO₂-600 indicate that the in-situ pyrolysis of metal-organic ligands not only embeds a rich array of C, N species into SiO₂ but

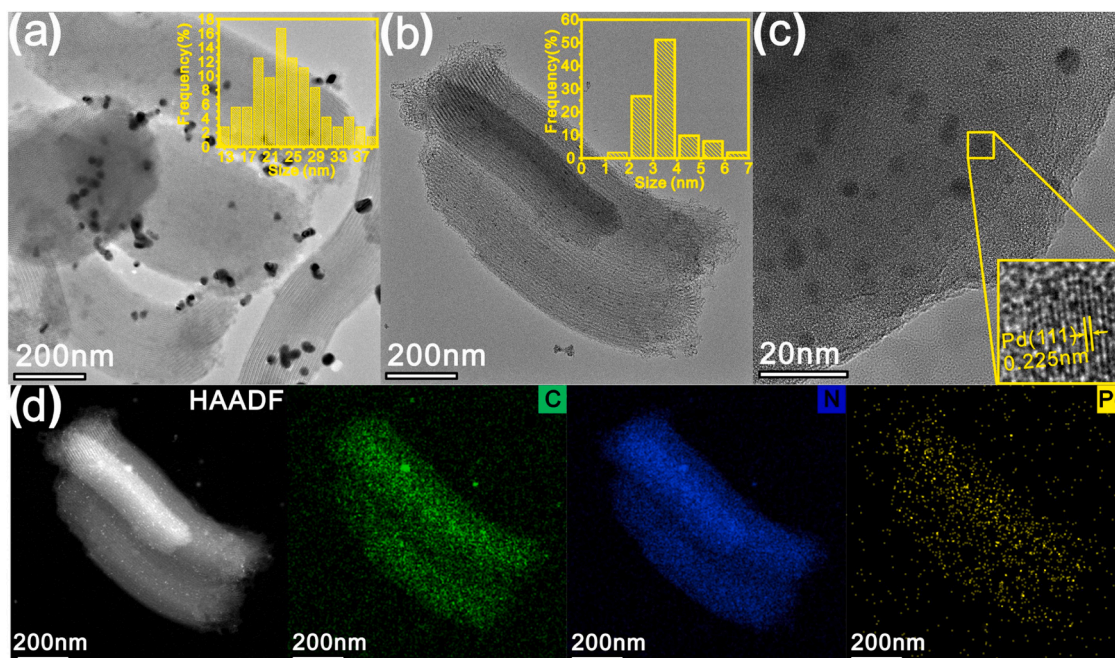


Fig. 1. (a-b) TEM images of Pd/SiO₂-600 and Pd-CN₂/SiO₂-600; (c) HRTEM images of Pd-CN₂/SiO₂-600; (d) Element mapping and energy spectrum of Pd-CN₂/SiO₂-600.

markedly augments the dispersion of Pd nanoparticles.

The pyrolysis temperature profoundly impacts the comprehensive structure and surface attributes of C-N materials, thereby directly influencing the efficacy of catalysts supported on such materials. Catalysts Pd-CN₂/SiO₂-Y, synthesized at varying pyrolysis temperatures, underwent characterization through N₂ physical adsorption-desorption, XRD, Raman, H₂-TPR, etc. As depicted in Fig. 2(a), both Pd-SiO₂-600 and Pd-CN₂/SiO₂-Y display Type IV isotherms [30], with H1 type hysteresis loops observed in the 0.6–0.8 P/P₀ range and distinct saturation adsorption plateaus in the 0.9–1.0 P/P₀ range. These findings suggest that the catalysts, across different pyrolysis temperatures, are mesoporous materials featuring organized pore structures. Data regarding the corresponding surface area, pore volume, and pore diameter are cataloged in Table S1. An increase in pyrolysis temperature leads to a gradual decrement in the saturation adsorption capacity of N₂, indicative of a pore number reduction. This may be associated with the dehydration reaction of SiO₂ at elevated temperatures, resulting in structural contraction. As evidenced in Figure S3, post-calcination at 800 °C, SiO₂'s surface area, pore volume, and pore diameter undergo significant reductions.

Relative to SiO₂, the surface area and pore volume of Pd/SiO₂-600 are diminished by 33 m²/g and 0.08 cm³/g, respectively, essentially maintaining stability. Conversely, the surface area and pore volume for Pd-CN₂/SiO₂-600 are reduced by 104 m²/g and 0.16 cm³/g, respectively. This pattern indicates that the integration of the C-N layer and Pd nanoparticles within the SiO₂ pores leads to a decrease in the catalyst's surface area and pore volume. This observation aligns with TEM findings, where only a limited number of small Pd nanoparticles are visible on the surface of Pd-CN₂/SiO₂-600, underscoring the effective

dispersion facilitated by the C-N layer.

X-ray diffraction (XRD) results for the catalysts with different pyrolysis temperatures, as presented in Fig. 2(c), identify characteristic diffraction peaks at 21.9° and 40.1° in Pd/SiO₂-600, corresponding to the signature diffraction peaks of SiO₂ (PDF#29-0085) [31] and the Pd (111) crystal plane (PDF#89-4897) [32,33], respectively. In contrast to Pd/SiO₂-600, Pd-CN₂/SiO₂-Y shows no detectable diffraction peaks for Pd species, indicating an enhanced dispersion of Pd within Pd-CN₂/SiO₂-Y. Table 1 shows Pd loading and metal dispersion of catalysts obtained at different pyrolysis temperatures. ICP-OES results reveal that the actual loadings of all catalysts hover around 0.85 wt%. CO pulse adsorption results indicate a metal Pd dispersion of 7.17% in

Table 1

Pd loading and metal dispersion of catalysts obtained at different pyrolysis temperatures.

Catalysts	Theoretical Pd loading (wt%)	Actual Pd loading ^a (wt%)	Pd dispersion ^b (%)	Pd particle size ^b nm
Pd/SiO ₂ -600	1.0	0.83	7.17	15.6
Pd-CN ₂ /SiO ₂ -500	1.0	0.84	64.67	1.7
Pd-CN ₂ /SiO ₂ -600	1.0	0.86	45.34	2.5
Pd-CN ₂ /SiO ₂ -700	1.0	0.85	40.15	2.8
Pd-CN ₂ /SiO ₂ -800	1.0	0.83	28.82	4.1

^a Determined by ICP-OES.

^b Calculated from CO pulse adsorption test results

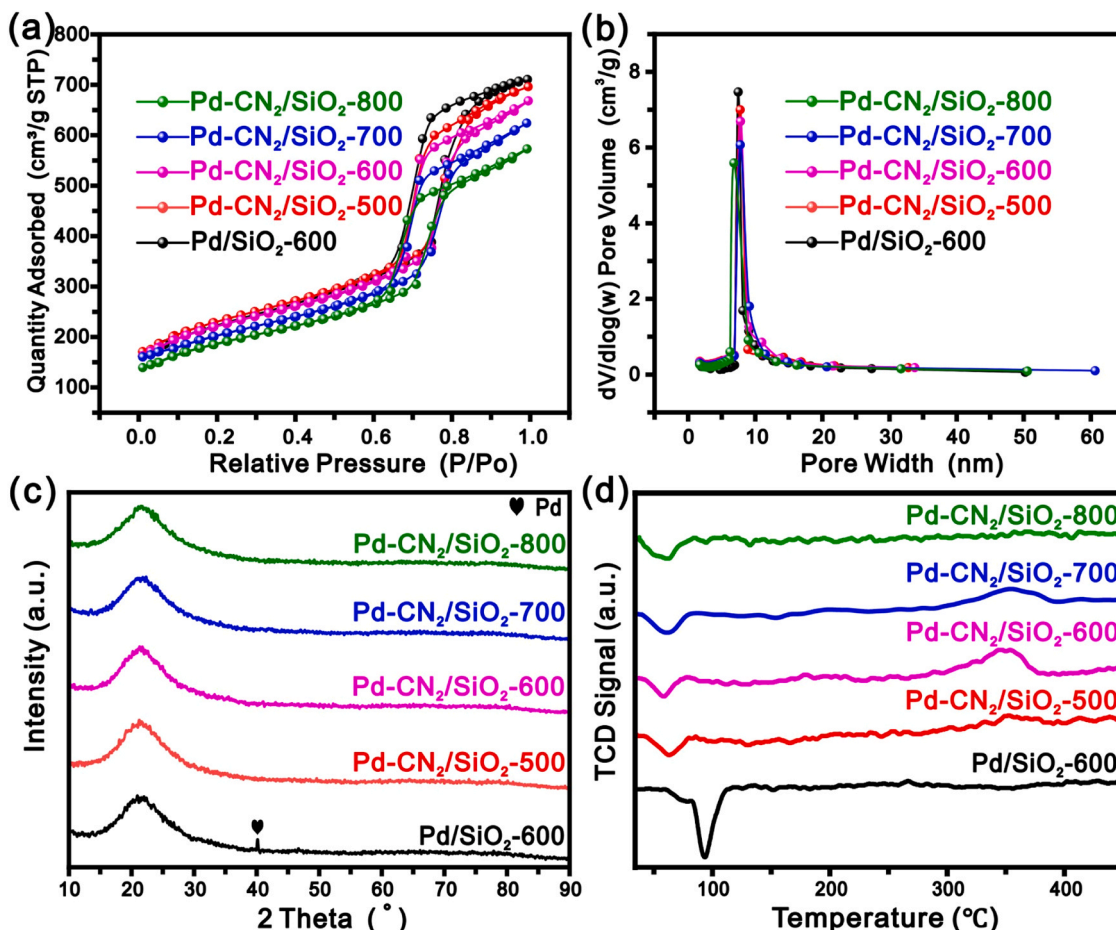


Fig. 2. The catalysts at different pyrolysis temperatures: (a) N₂ physical adsorption-desorption plots; (b) Pore size distribution plots; (c) XRD plots; (d) H₂-TPR plots.

Pd/SiO₂-600, which significantly increases to 45.34% in Pd-CN₂/SiO₂-600, with the particle size reducing from 15.6 nm to 2.5 nm. Concurrently, as the pyrolysis temperature rises, the C-N layer in Pd-CN₂/SiO₂-X begins to decompose, leading to enhanced Pd agglomeration. When the temperature reaches 800 °C, the metal dispersion drops to 28.82%, and the particle size increases to 4.1 nm. However, this is still significantly lower than the average particle diameter of 15.6 nm in Pd/SiO₂-600, suggesting that the Pd particles remain confined within the SiO₂ pore channels at this temperature. CO pulse adsorption findings suggest an increase in Pd nanoparticle diameter with escalating pyrolysis temperatures, potentially due to the influence of the C-N layer's thickness and defect sites on the catalyst surface.[34] Notably, at a pyrolysis temperature of 800 °C, Figure S2 reveals an absence of significant C layer peaks, implying that excessively high pyrolysis temperatures contribute to the C-N layer's decomposition. Nevertheless, the mean diameter of Pd nanoparticles in Pd-CN₂/SiO₂-800 stands at merely 4.1 nm, markedly less than the 15.6 nm average particle diameter observed in Pd/SiO₂-600, suggesting that Pd particles remain confined within the SiO₂ pores even at elevated pyrolysis temperatures.

The catalysts underwent hydrogen temperature-programmed reduction (H₂-TPR) to delve into the effects of varying pyrolysis temperatures on the interaction between the C-N layer and Pd nanoparticles. The peak manifesting in the 50–100 °C range, as shown in Fig. 2(d), is ascribed to the decomposition of β -PdH_x. [35] The genesis of β -PdH_x is profoundly influenced by the size of Pd nanoparticles, with larger particles more likely to form β -PdH_x. [36] Relative to Pd/SiO₂-600, a significant reduction in the decomposition peak area of β -PdH_x in

Pd-CN₂/SiO₂-Y points to a scarcity of large-sized Pd particles in Pd-CN₂/SiO₂-Y, aligning with XRD observations. Intriguingly, the incorporation of the C-N layer leads to the emergence of a reduction peak at 350 °C in Pd-CN₂/SiO₂-Y, peaking in intensity at a pyrolysis temperature of 600 °C. This peak, in comparison with the H₂-TPR spectrum of the CN₂/SiO₂-600 carrier depicted in Figure S4, is attributed to Pd^{δ+} species that exhibit a robust interaction with the C-N layer. These stable Pd^{δ+} species are found in abundance in Pd-CN₂/SiO₂-600. The collective findings from N₂ isotherm adsorption-desorption, XRD, and H₂-TPR analyses underscore the pivotal role of the strong interaction between the C-N layer and active metal Pd in promoting the formation of highly dispersed nanoparticles, effectively dual-confined both intra-pore and interfacial.

To further explore the impact of pyrolysis temperature on the electronic structure of Pd nanoparticles and the catalyst surface's acidity and basicity, we conducted characterizations using X-ray photoelectron spectroscopy (XPS), ammonia temperature-programmed desorption (NH₃-TPD), and hydrogen temperature-programmed desorption (H₂-TPD) on the Pd-CN₂/SiO₂-Y catalysts. The XPS analysis of Pd 3d orbitals, as depicted in Fig. 3(a), reveals a peak at 334.9 eV corresponding to Pd⁰ 3d_{5/2} and another at 336.6 eV associated with Pd²⁺ 3d_{5/2} in Pd/SiO₂-600. [37] The incorporation of the C-N layer introduces a novel peak around 335.6 eV, signaling the formation of a new chemical state of Pd within the C-N layer. It is widely recognized that Pd interacts strongly with pyridinic N present in the C-N layer, significantly affecting the carrier interaction. [38] Hence, the peak around 335.6 eV in Pd-CN₂/SiO₂-Y is designated to Pd^{δ+} species complexed with pyridinic N ($0 < \delta < 2$). Fig. 3(b) outlines the variation in N species within the C-N

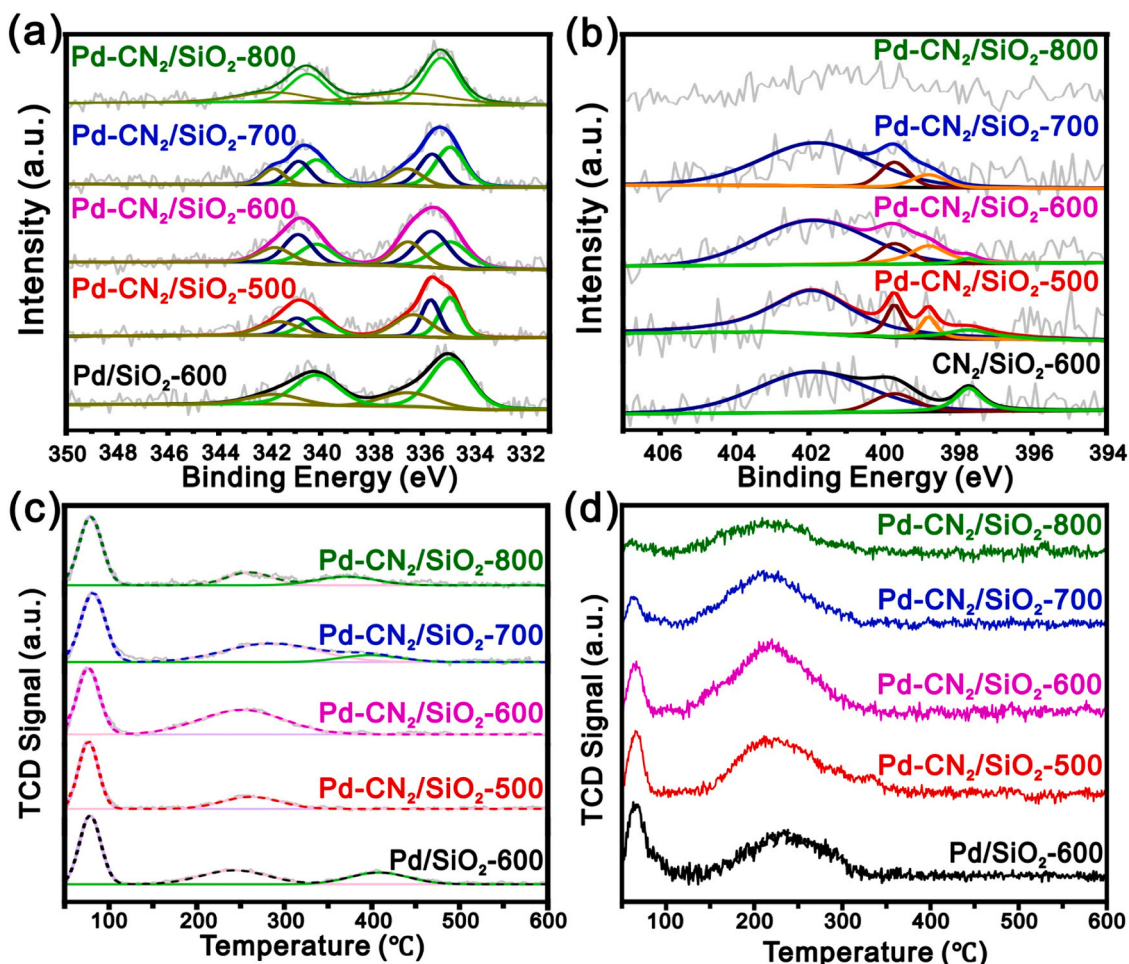


Fig. 3. The as-prepared catalysts at different pyrolysis temperatures: (a) Pd 3d orbital XPS plots; (b) N 1s orbital XPS plots; (c) NH₃-TPD plots (d) H₂-TPD plots.

layer across different pyrolysis temperatures, with peaks at 397.8 eV, 398.8 eV, 399.7 eV, and 401.9 eV corresponding to pyridinic N, Pd^{δ+}-pyridinic N, pyrrolic N, and graphitic N, respectively. [23] The analysis of Pd and N species of the as-prepared catalysts, detailed in Table S2 and S3, illustrates that the relative abundance of Pd^{δ+} species initially increases and then decreases with escalating pyrolysis temperature, reaching its apex in Pd-CN₂/SiO₂-600. Notably, the binding energy of Pd⁰ 3d_{5/2} in Pd-CN₂/SiO₂-800 is 335.2 eV, substantially higher than in Pd-CN₂/SiO₂-600, indicating that pyridinic N in the C-N layer forms stable Pd^{δ+} species through intense interaction with Pd.

The strong basicity of pyridinic N invariably influences the catalyst surface's acidity and basicity by its interaction with Pd nanoparticles. As illustrated in Fig. 3(c), Pd/SiO₂-600 exhibits NH₃ desorption peaks across < 100 °C, 200–300 °C, and 350–450 °C regions, denoting weak, medium, and strong acid sites on the catalyst surface, respectively. [39] The emergence of strong acid sites is attributed to the robust interaction between Pd and SiO₂. At pyrolysis temperatures of 500 °C and 600 °C, the disappearance of strong acid sites and the increase in medium acid site proportion are observed, attributed to the generation of Pd^{δ+}-pyridinic N species. With further increase in pyrolysis temperature, strong acid sites reemerge, suggesting the C-N layer's decomposition, a decline in Pd^{δ+}-pyridinic N species, and an intensified interaction between Pd and SiO₂. The distribution of acid sites of varying strengths within the catalyst is documented in Table 2, providing insights into the nuanced changes in surface chemistry as a function of pyrolysis temperature.

The stability of the catalyst surface toward hydrogen species is pivotal for influencing dehydrogenation reaction efficiency. The characterization results from hydrogen temperature-programmed desorption (H₂-TPD), showed in Fig. 3(d), elucidate this aspect. Desorption of hydrogen at lower temperatures is typically indicative of active sites on metallic Pd, whereas desorption at higher temperatures is associated with active sites on oxidized Pd. [40] Zhang et al. [41] have posited the phenomenon of hydrogen spillover on surfaces of noble metals, wherein hydrogen initially dissociates on metallic Pt sites and subsequently spills over to adjacent oxidized Pt sites for strong adsorption. Meng et al. [42] proposed that active sites on metallic Pd are instrumental in activating and dissociating C-H bonds in 4 H-NECZ, with the dissociated hydrogen species spilling over to oxidized Pd active sites for desorption. This synergistic interaction between metallic and oxidized Pd active sites is advantageous for the comprehensive dehydrogenation of 12 H-NECZ. It is noteworthy that although Pd-CN₂/SiO₂-800 features considerably smaller Pd nanoparticles compared to Pd/SiO₂-600, its desorption peaks in both the low and high-temperature zones are significantly diminished. Therefore, hydrogen desorption below 100 °C in Pd-CN₂/SiO₂-Y is ascribed to hydrogen species adsorbed on Pd⁰, while hydrogen desorption around 230 °C is ascribed to hydrogen species adsorbed on Pd^{δ+}, stabilized by pyridinic N. Pd-CN₂/SiO₂-600 demonstrates the most substantial desorption peak areas in both the low and high-temperature ranges, signifying an abundant presence of both Pd⁰ and Pd^{δ+} species, thereby highlighting its enhanced capabilities in facilitating hydrogen adsorption and desorption processes.

To gain deeper insights into the geometric and electronic structure of Pd nanoparticles within the catalyst, CO Diffuse Reflectance Infrared Fourier Transform (DRIFT) spectroscopy was employed. The findings are illustrated in Fig. 4. The absorption peak at 2132 cm⁻¹ in Pd/SiO₂-

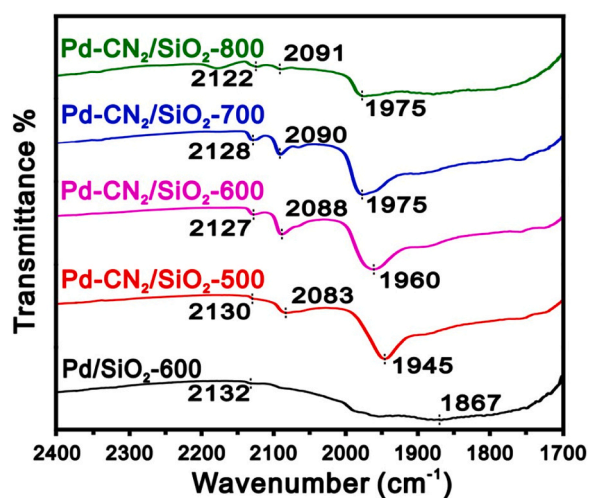


Fig. 4. CO-DRIFT characterization plots for catalysts with different pyrolysis temperatures.

600 corresponds to gaseous CO, whereas the peak at 1867 cm⁻¹ is indicative of CO's twin adsorption on metallic Pd. [43] This twin adsorption phenomenon is closely related to the size of Pd particles, with larger particles more likely to facilitate twin adsorption sites. [44] The introduction of the C-N layer leads to the disappearance of the 1867 cm⁻¹ absorption peak in Pd-CN₂/SiO₂-Y, signifying enhanced dispersion and a decrease in the size of Pd nanoparticles, a finding corroborated by TEM and XRD analyses.

Notably, Pd-CN₂/SiO₂-Y exhibits two distinct CO adsorption peaks within the 1900–2100 cm⁻¹ range. The peak at 2083 cm⁻¹ is ascribed to the linear adsorption of CO on Pd^{δ+} species, stabilized by pyridinic nitrogen. [16,42,43] The intensity of this peak initially increases and then decreases with rising pyrolysis temperatures, reaching its maximum in Pd-CN₂/SiO₂-600. This trend implies the most prolific presence of Pd^{δ+} species in this specific catalyst variant.

The peaks observed between 1945 and 1975 cm⁻¹ are attributed to the bridge adsorption of CO on small-sized Pd nanoparticles. [16,42] An increase in pyrolysis temperature leads to a shift of these peaks towards higher wavenumbers, signifying a diminishing interaction between Pd nanoparticles and CO's π -bonds, thereby weakening CO adsorption strength. In Pd-CN₂/SiO₂-800, the intensity of CO adsorption peaks is markedly weaker compared to other catalysts, indicating the vanishing C-N layer and a reduced interaction between Pd nanoparticles and π -bonds, potentially because of their encapsulation within SiO₂ pores. [45,46] It is widely recognized that catalyst activity and reactant adsorption strength share a volcano-type relationship, where optimal adsorption strength is the key for adequate reactant activation and efficient product release.

Furthermore, the ratio of the Pd precursor to the phenanthroline ligand emerges as a critical determinant of catalyst structure and functionality. The structural features of catalysts synthesized with varying phenanthroline to Pd precursor ratios are detailed in Figure S5 and Table S4-S7. N₂ adsorption-desorption characterizations indicate that variations in ligand ratio exert minimal influence on the catalyst's pore architecture. Results from XRD and CO pulse adsorption analyses reveal a notable decrease in Pd nanoparticle size with increasing phenanthroline ratios. Beyond a ligand ratio of 0.5, changes in nanoparticle size become less distinct. H₂-TPR and XPS findings demonstrate that a ligand to precursor ratio of 2 leads to the formation of stable Pd^{δ+} species, showcasing robust interactions with the C-N layer, thereby influencing the catalyst's performance and structural integrity. It should be noted that maintaining a constant ratio of phenanthroline to Pd and pyrolysis temperature, excessive Pd loading results in significant nanoparticle agglomeration. This not only inhibits the formation of Pd^{δ+} species, but

Table 2
Distribution and content of acidic sites by region in different catalysts.

Catalysts	Acid composition		
	Weak	Intermediate	Strong
Pd/SiO ₂ -600	78 °C (47%)	242 °C (30%)	408 °C (23%)
Pd-CN ₂ /SiO ₂ -500	77 °C (66%)	261 °C (34%)	–
Pd-CN ₂ /SiO ₂ -600	76 °C (41%)	251 °C (59%)	–
Pd-CN ₂ /SiO ₂ -700	82 °C (43%)	285 °C (45%)	398 °C (12%)
Pd-CN ₂ /SiO ₂ -800	79 °C (59%)	260 °C (23%)	370 °C (18%)

also diminishes the dehydrogenation activity of the catalyst. The structural characterization and dehydrogenation performance of catalysts with varying Pd loadings are detailed in Figure S7. Notably, the results from the dehydrogenation studies indicate that the catalyst achieves optimal activity at a Pd loading of 1 wt%.

3.2. Catalytic dehydrogenation evaluation

To examine the impact of different pyrolysis temperatures and phenanthroline ligand ratios on catalytic efficiency, we conducted a thorough assessment of the dehydrogenation activities of the Pd-CN_x/SiO₂-Y series of catalysts, as illustrated in Fig. 5(a) and Figure S6. Among these, Pd-CN₂/SiO₂-600 showcased outstanding catalytic performance, achieving the complete dehydrogenation of 12 H-NPCZ in just 240 minutes. This remarkable dehydrogenation rate is attributed to the finely dispersed Pd⁰ nanoparticles and the plentiful Pd^{δ+}-pyridinic N species within the catalyst. Interestingly, Pd-CN₂/SiO₂-800's dehydrogenation activity was markedly lower than that of Pd/SiO₂-600, a difference likely due to the spatial confinement of Pd nanoparticles within the SiO₂ matrix. Characterizations including H₂-TPD and CO-DRIFT analyses have pointed out that Pd-CN₂/SiO₂-800 exhibited substantially weaker interactions with hydrogen species and reactants containing π-bonds than its counterparts.

The product distributions of 12 H-NPCZ dehydrogenation catalyzed by Pd/SiO₂-600, Pd-CN₂/SiO₂-600, and Pd-CN₂/SiO₂-800 catalysts are detailed in Fig. 5(b-d). The dehydrogenation process of 12 H-NPCZ adheres to a sequential pathway: 12 H-NPCZ → 8 H-NPCZ → 4 H-NPCZ → NPCZ, with the conversion of 4 H-NPCZ to NPCZ constituting the rate-determining step of the entire process. [15,47,48] The

efficiency of conversion from 12 H-NPCZ to 8 H-NPCZ among the catalysts ranked as follows: Pd-CN₂/SiO₂-600 > Pd/SiO₂-600 > Pd-CN₂/SiO₂-800. This ranking may be ascribed to the strong acid sites present on the catalyst surface, where the basic N atom in the five-membered ring of 12 H-NPCZ interacts too vigorously with the strong acid sites of Pd/SiO₂-600 and Pd-CN₂/SiO₂-800, thereby impeding the dehydrogenation process.

The cyclic stability of a catalyst is a pivotal parameter when assessing its performance and potential applications. In our study, we evaluated the cyclic dehydrogenation capabilities of Pd-CN₂/SiO₂-600 and Pd/SiO₂-600. Fig. 6(a) illustrate that the catalytic activity of Pd-CN₂/SiO₂-600 remains consistent, even after 10 continuous cycles, successfully achieving the complete dehydrogenation of 12 H-NPCZ. Conversely, Pd/SiO₂-600 exhibits a noticeable decline in dehydrogenation activity as the number of cycles increases, as shown in Fig. 6(b). The purity of the dehydrogenation gas from 12 H-NPCZ catalyzed by Pd-CN₂/SiO₂-600 was assessed using mass spectrometry. The results, presented in Figure S8, revealed that no other gas components were detected besides H₂. This indicates that Pd-CN₂/SiO₂-600 exhibits excellent selectivity in catalyzing the dehydrogenation of 12 H-NPCZ.

The N₂-isothermal adsorption-desorption curve and the XRD pattern of Pd-CN₂/SiO₂-600, after undergoing 10 dehydrogenation cycles, are depicted in Figure S9. These results indicate that there are no significant changes in the pore properties and the bulk structure of the catalyst, suggesting that the SiO₂ support exhibits excellent stability during dehydrogenation.

The particle size variations of the catalysts pre and post-cycling are depicted in Fig. 6(e-f). After 10 cycles, the particle size distribution of Pd-CN₂/SiO₂-600 becomes more diverse, with the majority of particles

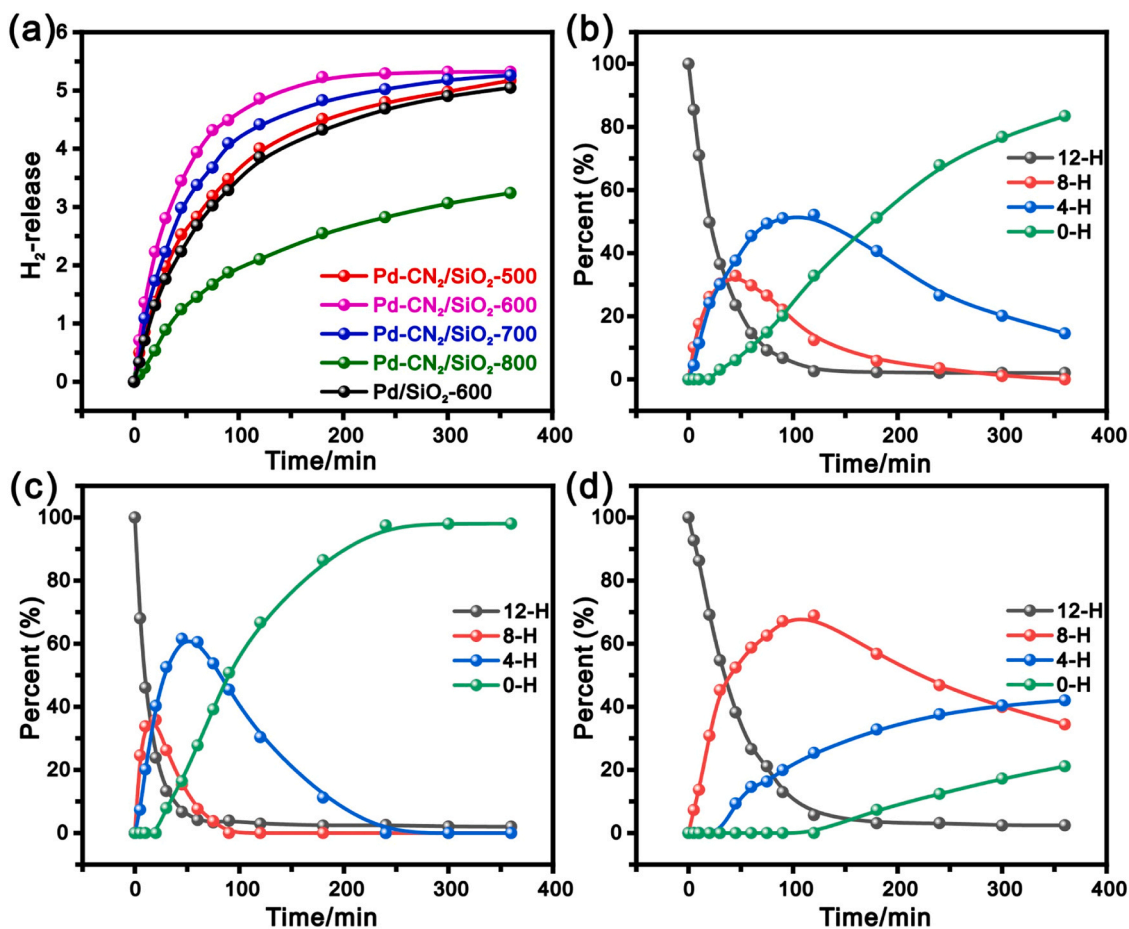


Fig. 5. (a) Hydrogen release curves of Pd-CN₂/SiO₂-X and Pd/SiO₂-600 catalysts; (b) Variation of dehydrogenation products of Pd/SiO₂-600; (c) Variation of dehydrogenation products of Pd-CN₂/SiO₂-600; (d) Variation of dehydrogenation products of Pd-CN₂/SiO₂-800.

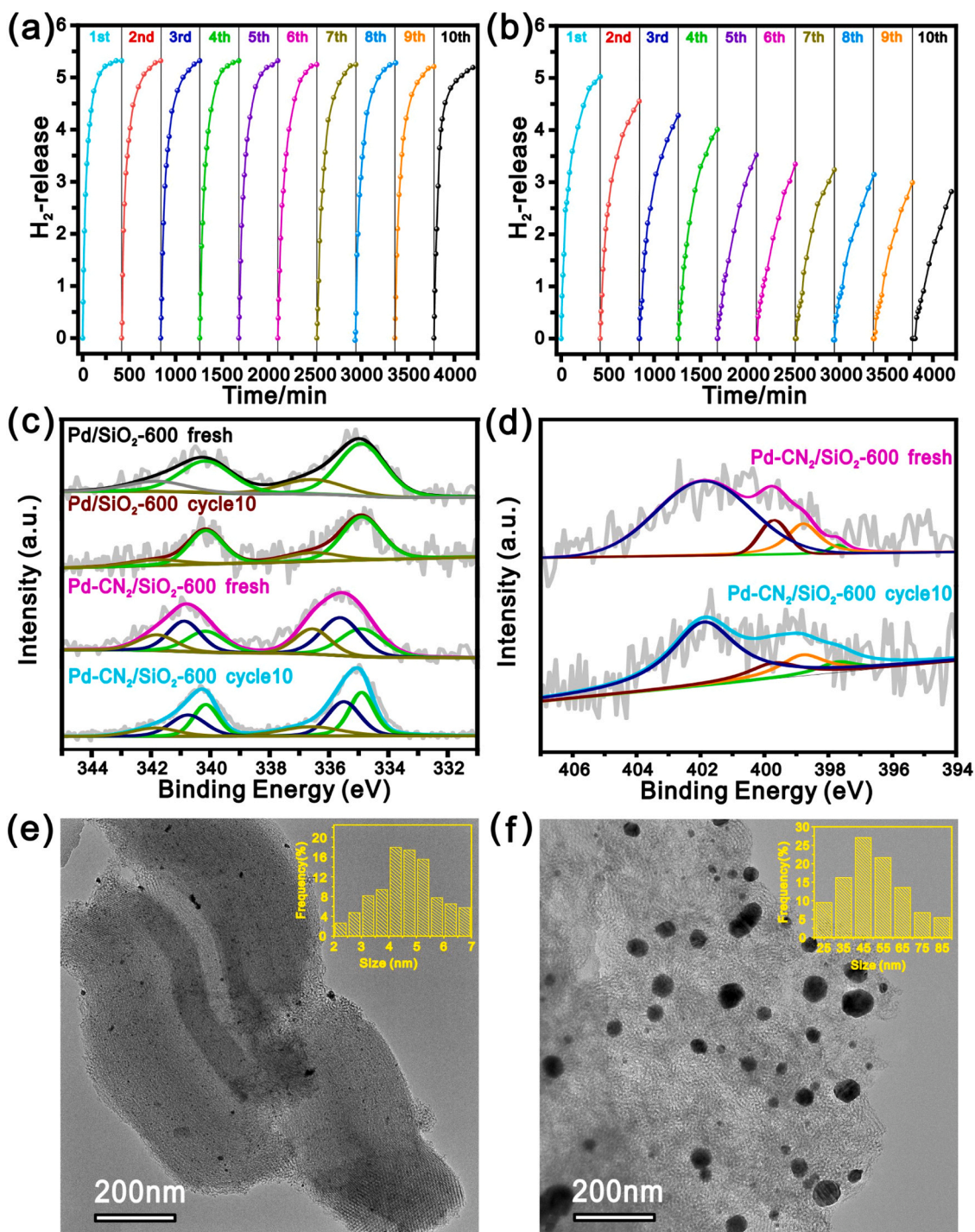


Fig. 6. (a-b) Comparison curves of 10 dehydrogenation cycles over Pd-CN₂/SiO₂-600 and Pd/SiO₂-600 catalysts; (c) Pd 3d orbital XPS images; (d) N 1 s orbital XPS images; (e-f) TEM images of Pd-CN₂/SiO₂-600, Pd/SiO₂-600 catalysts after 10 cycles.

falling within the 4–6 nm range, a slight increase from the pre-cycling measurements. On the other hand, the particle size of Pd/SiO₂-600 expands to 45–55 nm, indicating a significant agglomeration compared to its pre-cycling state.

The XPS characterization results, as shown in Fig. 6(c-d) and Table 3, reveal a decrease in the Pd²⁺ content and an increase in the Pd⁰ content in Pd/SiO₂-600 after cycling. However, in Pd-CN₂/SiO₂-600, the Pd⁶⁺-pyridine N species content remains virtually unchanged, as does the signal intensity of the C-N layer and the content of various N species. These observations underscore the stability of the C-N layer and Pd⁶⁺-pyridine N species throughout the cycling process.

Table 3

Binding energy and relative content of different types of Pd for different catalysts before and after cycling.

Sample	Binding Energy Pd (eV)		
	Pd ⁰ 3d _{5/2}	Pd ⁶⁺ 3d _{5/2}	Pd ²⁺ 3d _{5/2}
Pd-CN ₂ /SiO ₂ -600 fresh	334.9 (20%)	335.6 (25%)	336.6 (15%)
Pd-CN ₂ /SiO ₂ -600 cycle10	334.9 (25%)	335.5 (24%)	336.6 (11%)
Pd/SiO ₂ -600 fresh	334.9 (44%)	–	336.6 (16%)
Pd/SiO ₂ -600 cycle10	334.9 (48%)	–	336.6 (12%)

In essence, the exceptional stability of Pd-CN₂/SiO₂-600 is credited to the C-N layer's effective anchoring of Pd nanoparticles, preventing agglomeration throughout the cycling. Additionally, the persistent stability of both the carbon-nitrogen layer and Pd^{δ+}-pyridinic N species guarantees sustained high activity for the dehydrogenation reaction over multiple cycles.

3.3. Catalytic dehydrogenation mechanism

Through kinetic experimentation, we delved into 12 H-NPCZ dehydrogenation reaction mechanism for Pd-CN₂/SiO₂-600 and Pd/SiO₂-600 catalysts. The full dehydrogenation process of 12 H-NPCZ comprises three sequential stages: 12 H-NPCZ to 8 H-NPCZ, then to 4 H-NPCZ, and finally to NPCZ, each treated as a first-order reaction. Kinetic rates for these catalysts were assessed across a temperature spectrum of 180–210 °C, with their respective activation energies computed via the Arrhenius

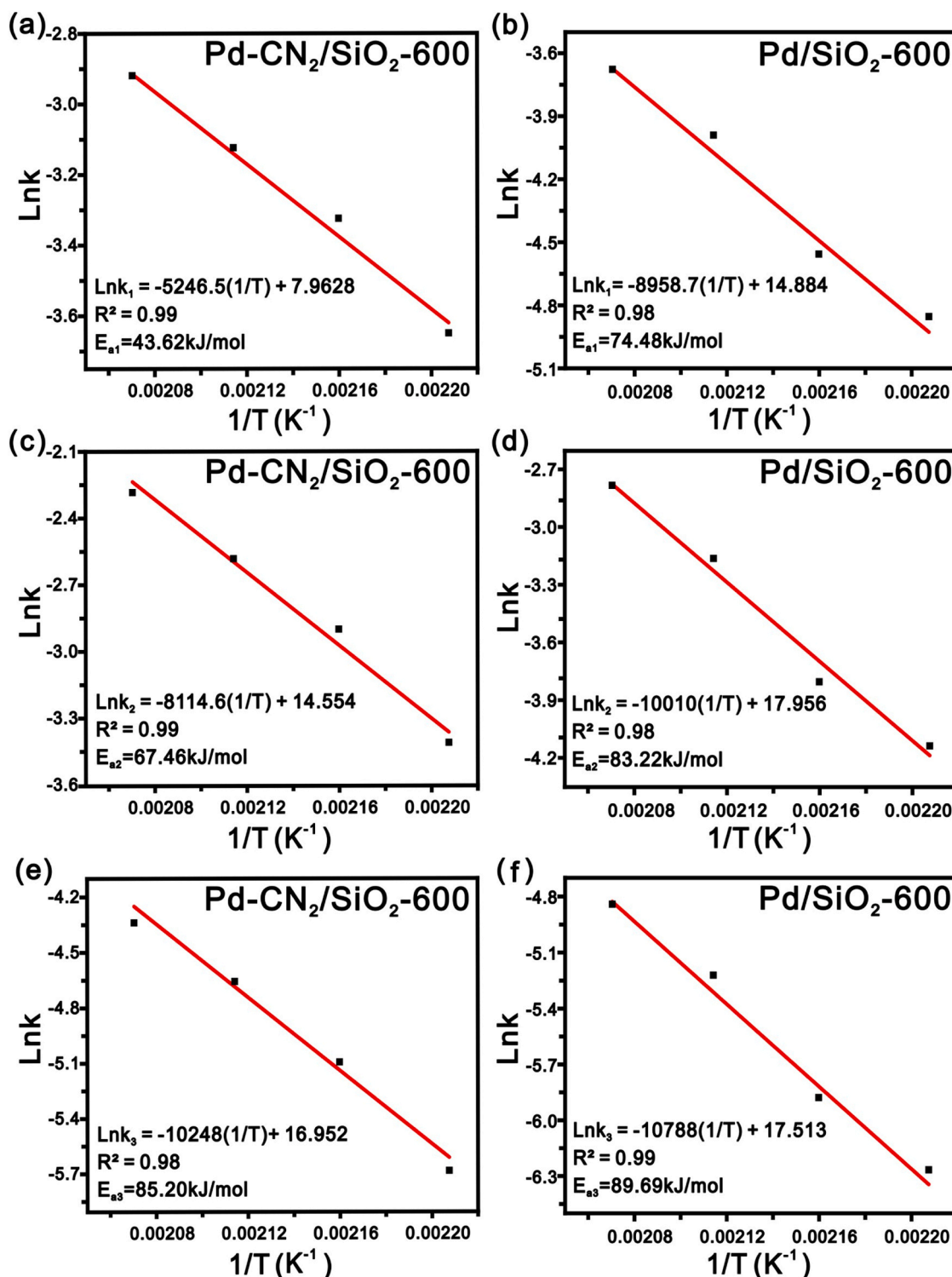


Fig. 7. Arrhenius plots of catalyst-catalyzed 12 H-NPCZ dehydrogenation at 180–200 °C: (a, c, e) Pd-CN₂/SiO₂-600; (b, d, f) Pd/SiO₂-600.

equation, as elaborated in the [Supporting Information](#) section. As shown in [Fig. 7](#), Pd-CN₂/SiO₂-600 showcased activation energies of $E_{a1}=43.62$ kJ/mol, $E_{a2}=67.46$ kJ/mol, and $E_{a3}=85.20$ kJ/mol for its three dehydrogenation stages. Comparatively, Pd/SiO₂-600 presented activation energies of $E_{a1}=74.48$ kJ/mol, $E_{a2}=83.22$ kJ/mol, and $E_{a3}=89.69$ kJ/mol. The notably reduced E_{a1} and E_{a2} for Pd-CN₂/SiO₂-600, as opposed to Pd/SiO₂-600, signify that Pd-CN₂/SiO₂-600 effectively lowers the energy barriers across the dehydrogenation pathway, especially pronounced in the conversion from 12 H-NPCZ to 8 H-NPCZ.

To better compare the catalytic effects with other similar Pd-based catalysts, we have compiled the activation energy data for the dehydrogenation of 12 H-NPCZ/12 H-NECZ catalyzed by supported Pd catalysts as reported in the literature. The relevant data is presented in [Table 4](#). In fact, Pd-CN₂/SiO₂-600 exhibits a lower E_{a1} than most reported Pd-based catalysts. Furthermore, the actual loading of Pd in the synthesized Pd-CN₂/SiO₂-600 in this study is only 0.86 wt%, significantly lower than that of the reported catalysts. Compared to other reported catalysts, the Pd-CN₂/SiO₂-600 catalyst demonstrates a faster hydrogen production rate from 12 H-NPCZ per unit mass of the precious metal Pd and exhibits a higher efficiency in Pd atom utilization. This increased efficiency implies that the Pd-CN₂/SiO₂-600 catalyst achieves significant catalytic activity with lesser amounts of the precious metal, which is a crucial attribute in catalysis, reflecting both economic and environmental benefits.

DFT calculations were performed to elucidate the electron distribution on Pd nanoparticles within Pd/SiO₂-600 and Pd-CN₂/SiO₂-600 catalysts. The analysis, depicted in [Fig. 8\(a, d\)](#), reveals a concentration of charges on Pd nanoparticles in Pd/SiO₂-600. In contrast, Pd-CN₂/SiO₂-600 shows charges dispersed near the nanoparticle and C-N layer interface. Bader charge analysis indicated that the average Bader charges for Pd on the surface of Pd/SiO₂-600 were 10.09, while for Pd on Pd-CN₂/SiO₂-600, it was 9.88. This assessment of the electronic structure proves an electron migration from Pd clusters towards the CN layer in Pd-CN₂/SiO₂-600, aligning with XPS characterization findings. The incorporation of the C-N layer fosters an interaction between Pd and pyridinic nitrogen, facilitating electron transfer from Pd to N and leading to the formation of an abundance of Pd^{δ+} species, stabilized by pyridinic N at the active metal-support interface.

The projected density of states (PDOS) on the surfaces of Pd/SiO₂-600 and Pd-CN₂/SiO₂-600, as illustrated in [Fig. 8\(b, e\)](#), demonstrate a significant downward shift of the d-band center of Pd in Pd-CN₂/SiO₂-600 away from the Fermi level, relative to Pd/SiO₂-600. In the realm of transition metal catalysis, proximity of the d-band center to the Fermi level is typically associated with enhanced adsorptive interactions. However, overly strong adsorption tendencies could potentially lead to catalyst poisoning and subsequent deactivation.[\[56\]](#) Meng et al. have highlighted that in the dehydrogenation processes, particularly for 12 H-NECZ, the desorption of intermediate reaction products from the active sites crucially dictates the dehydrogenation rate, overshadowing

the activation of C-H bonds in terms of significance.[\[42\]](#)

The side views of 12 H-NPCZ, 8 H-NPCZ, 4 H-NPCZ and NPCZ adsorbed on the catalyst surface are shown in [Figure S10](#). The data of adsorption energies of different adsorbates on the catalyst surface are listed in [Table S8](#). In-depth analyses into the adsorption behaviors of various intermediates on the surfaces of Pd/SiO₂-600 and Pd-CN₂/SiO₂-600 revealed markedly lower adsorption energies for intermediates on Pd-CN₂/SiO₂-600. This phenomenon suggests a faster desorption rate from the catalyst's active sites, thereby accelerating the dehydrogenation process. Notably, the adsorption energy of 8 H-NPCZ on Pd-CN₂/SiO₂-600 was found to be significantly lower than that of 12 H-NPCZ, which may be attributed to differing adsorption mechanisms. The pronounced basicity of the lone pair electrons on the N atom within the five-membered ring of 12 H-NPCZ results in a predominance of acid-base type adsorption. Conversely, the lone pair electrons of N atom within the five-membered ring of 8 H-NPCZ, 4 H-NPCZ and NPCZ contribute to the aromatic conjugation of the pyrrole ring. This involvement diminishes the accessibility of the lone pair electrons, consequently attenuating the basicity of these intermediates. Furthermore, intermediates featuring π -bonds potentially engage in complex adsorption with transition metals, where the adsorption strength is contingent upon the intensity of d- π back-donation. The introduction of the C-N layer markedly diminishes the acidity on the surface of Pd-CN₂/SiO₂-600, concurrently reducing the intensity of d- π back-donation, thereby decreasing the adsorption energy of the adsorbates.

Further, we have calculated the reaction energies for the sequential dehydrogenation stages of 12 H-NPCZ to 8 H-NPCZ, 8 H-NPCZ to 4 H-NPCZ, and 4 H-NPCZ to NPCZ on different catalysts, as illustrated in [Fig. 8\(c, f\)](#). For the Pd-CN₂/SiO₂-600 catalyst, the reaction energies for these three dehydrogenation stages are $\Delta H_1 = 1.18$ eV, $\Delta H_2 = 1.28$ eV, and $\Delta H_3 = 1.48$ eV, respectively. In comparison, the reaction energies for the Pd/SiO₂-600 catalyst for the same dehydrogenation steps are $\Delta H_1 = 1.49$ eV, $\Delta H_2 = 1.54$ eV, and $\Delta H_3 = 1.72$ eV, respectively. These findings are in alignment with the activation energy results and confirm that the Pd-CN₂/SiO₂-600 catalyst effectively reduces the reaction energies, thereby facilitating the progression of the reaction. This correlation between reduced reaction energies and enhanced catalytic performance underscores the effectiveness of Pd-CN₂/SiO₂-600 in promoting dehydrogenation processes, highlighting its potential for efficient catalysis.

The dehydrogenation process of 12 H-NPCZ, facilitated by Pd nanoparticles confined within a C-N layer, is modeled based on the provided analysis and depicted in [Fig. 9](#). The process initiates with the adsorption of 12 H-NPCZ at the interface of Pd and the C-N layer, where Pd⁰ active sites activate the C-H bonds. This leads to the generation of 8 H-NPCZ, which subsequently detaches from the Pd-C-N interface. The strong adsorption by Pd⁰ active sites continues to activate C-H bonds, resulting in the sequential formation of 4 H-NPCZ and ultimately NPCZ. Simultaneously, hydrogen species generated during the

Table 4
Apparent activation energies and dehydrogenation rates for 12 H-NPCZ/NECZ with different catalysts.

Catalysts	Pd loading(wt%)	Hydrogen storage materials	Hydrogen release rate (g _{H2} ·g _{cat} ⁻¹ ·min ⁻¹)	activation energy (kJ/mol)			References
				E_{a1}	E_{a2}	E_{a3}	
Pd-CN ₂ /SiO ₂ -600	1.0	12 H-NPCZ	0.335	43.62	67.46	85.20	This work
Pd/SiO ₂ -600	1.0	12 H-NPCZ	0.219	74.48	83.22	89.69	This work
Pd/Al ₂ O ₃	5.0	12 H-NPCZ	0.110	90.00	90.60	96.40	[49]
Pd@MIL-101	3.0	12 H-NPCZ	0.463	94.80	95.90	98.80	[50]
Pd-EU/K6	1.0	12 H-NECZ	0.255	73.80	—	—	[51]
Pd-Ni/Al ₂ O ₃	2.5	12 H-NPCZ	0.066	72.03	—	—	[14]
Pd/20%Ce-Al ₂ O ₃	1.0	12 H-NPCZ	0.347	—	—	—	[35]
Pd ₃ Au ₁ /SiO ₂	3.8	12 H-NECZ	0.284	—	—	—	[52]
Pd ₃ Ni ₁ /SiO ₂	3.9	12 H-NECZ	0.294	—	—	—	[53]
Pd/rGo	2.3	12 H-NECZ	0.285	—	—	—	[11]
Pd/rGO-EG	2.5	12 H-NPCZ	0.100	—	—	—	[54]
Pd/TiO ₂	5.0	12 H-NECZ	0.143	—	—	—	[55]

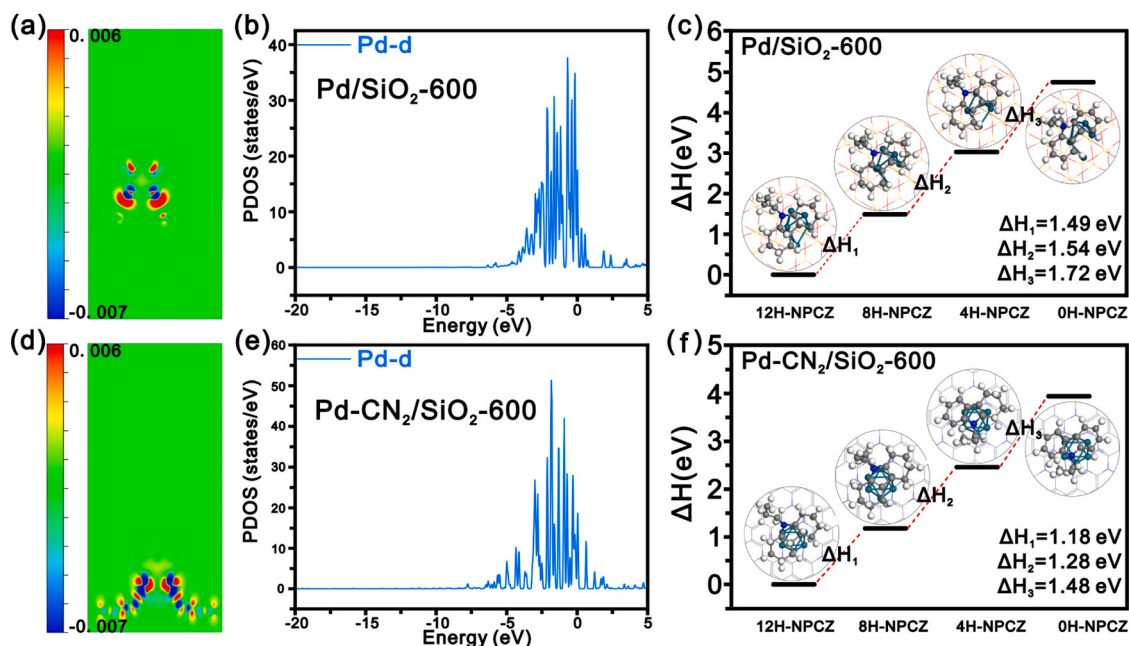


Fig. 8. Pd/SiO₂-600 and Pd-CN/SiO₂-600 catalysts: (a, d) Two-dimensional display of differential charge density on the surface; (b, e) Planar average differential charge density map; (c, f) Reaction energy diagram for the dehydrogenation of 12 H-NPCZ.

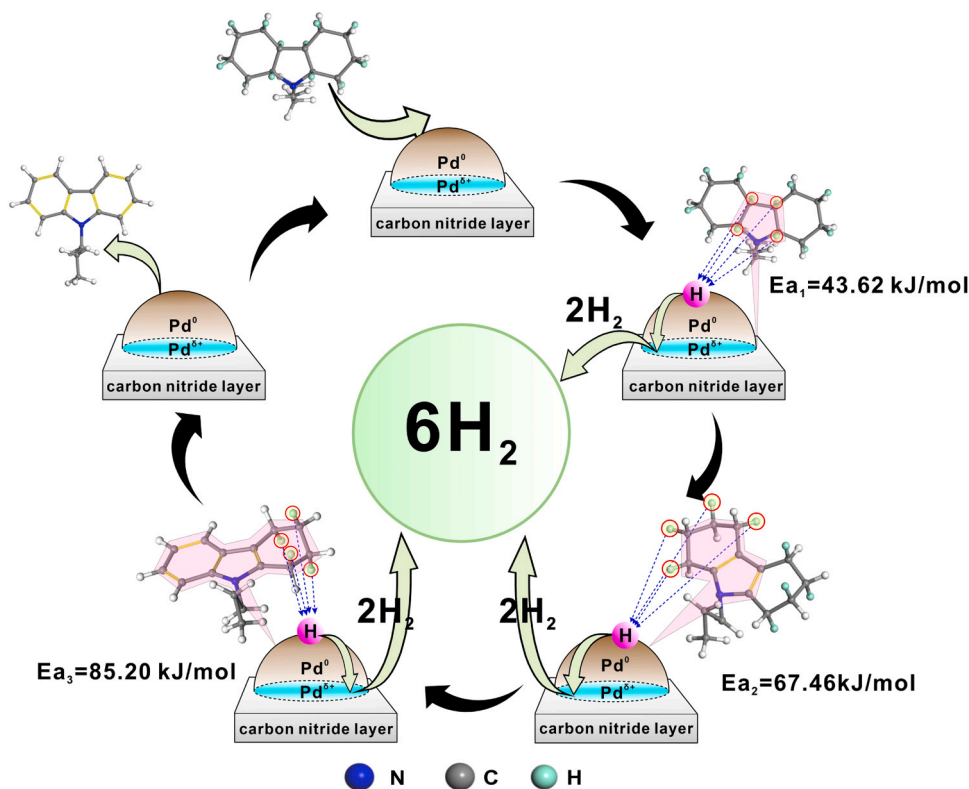


Fig. 9. Schematic illustration of the dehydrogenation reaction mechanism of 12 H-NPCZ on Pd-CN₂/SiO₂-600.

dehydrogenation process spillover from Pd⁰ active sites to Pd^{δ+} active sites situated at the Pd-C-N interface. This transition facilitates the desorption of hydrogen species, thereby liberating active sites for continuous dehydrogenation activity.

4. Conclusion

This study introduces a novel approach for incorporating Pd nanoparticles into the well-ordered pores of SiO₂, utilizing N-containing organic ligands. Through a process of high-temperature pyrolysis, we synthesize nano Pd-based catalysts encapsulated by a C-N layer. These catalysts demonstrate remarkable catalytic activity and superior cyclic

stability in the dehydrogenation of 12 H-NPCZ. The C-N layer plays a crucial role in enhancing the dispersion of Pd nanoparticles and effectively mitigates the formation of strong acid sites within the catalyst structure. The synergistic interaction between the C-N layer and Pd nanoparticles crucially modifies the electronic state of the Pd⁰ active sites and the adsorption dynamics of reaction intermediates, consequently impacting the dehydrogenation efficiency of the catalyst. By meticulously adjusting the pyrolysis temperature and the ratio of the ligands, we can fine-tune the interaction between the C-N layer and Pd nanoparticles. This adjustment leads to the formation of pyridinic nitrogen-stabilized Pd^{δ+} species at the metal-support interface, which are instrumental in providing acid sites of optimal strength. These sites facilitate the adsorption of 12 H-NPCZ and 8 H-NPCZ, thereby promoting the dehydrogenation process. Furthermore, these Pd^{δ+} species offer additional spillover sites for hydrogen species produced during dehydrogenation, which accelerates the desorption of reaction products from the active sites. This mechanism significantly enhances the catalyst's intrinsic activity for the dehydrogenation of 12 H-NPCZ. Through a comprehensive understanding of the interaction between catalyst components and the controlled modification of catalyst properties, we offer valuable insights and guidance for advancing the field of catalysis, particularly in the development of efficient LOHCs dehydrogenation catalysts.

CRedit authorship contribution statement

Chenggen Li: Writing – review & editing, Formal analysis, Data curation. **Yinheng Zhao:** Methodology, Data curation. **Qingyang Zhang:** Writing – original draft, Investigation, Formal analysis. **Chengwei Deng:** Writing – review & editing, Supervision, Conceptualization. **Li Liu:** Writing – original draft, Investigation, Formal analysis. **Hansong Cheng:** Supervision, Conceptualization. **Ming Yang:** Writing – review & editing, Supervision, Funding acquisition, Conceptualization. **Yuan Dong:** Writing – review & editing, Supervision, Funding acquisition. **Rongyi Gao:** Writing – original draft, Formal analysis, Data curation. **Ting Zhu:** Supervision, Investigation, Funding acquisition, Formal analysis.

Declaration of Competing Interest

The authors declare that they have no known competing financial interests or personal relationships that could have appeared to influence the work reported in this paper.

Data availability

Data will be made available on request.

Acknowledgements

The authors gratefully acknowledge the financial support from the Key Research and Development Program of Hubei Province (No. 2022BAA091 and 2023BAB162) and China University of Geosciences (Wuhan) for a program of the Central University Outstanding Youth Team.

Supporting information

SiO₂ preparation process; 12 H-NPCZ preparation process; Kinetics Calculation Methods; Raman plots of Pd-CN₂/SiO₂-Y catalysts; N₂ physical adsorption and desorption curves and pore size distributions of SiO₂ and SiO₂-800 carriers; Structural characterization results and dehydrogenation performance results of Pd-CN_x/SiO₂-600 catalysts; Structural models of all reaction intermediates on catalysts surfaces; Specific surface area, pore structure parameters, and binding energy and relative content of Pd and N in catalysts at different pyrolysis

temperatures; Specific surface area, pore structure parameters, binding energy and relative content of Pd and N, and Pd loading and metal dispersion in catalysts with different ligand ratios; Adsorption energy of each adsorbate on the surface of Pd/SiO₂-600 and Pd-CN/SiO₂-600 catalysts.

Appendix A. Supporting information

Supplementary data associated with this article can be found in the online version at doi:10.1016/j.apcatb.2024.123987.

References

- [1] C. Tarhan, M.A. Çil, A study on hydrogen, the clean energy of the future: hydrogen storage methods, *J. Energy Storage* 40 (2021) 102676–102685.
- [2] B. Johnston, M.C. Mayo, A. Khare, Hydrogen: the energy source for the 21st century, *Technovation* 25 (2005) 569–585.
- [3] D.K. Ross, Hydrogen storage: the major technological barrier to the development of hydrogen fuel cell cars, *Vacuum* 80 (2006) 1084–1089.
- [4] Q.-L. Zhu, Q. Xu, Liquid organic and inorganic chemical hydrides for high-capacity hydrogen storage, *Energy Environ. Sci.* 8 (2015) 478–512.
- [5] P. Preuster, C. Papp, P. Wasserscheid, Liquid organic hydrogen carriers (LOHCs): toward a hydrogen-free hydrogen economy, *Acc. Chem. Res.* 50 (2017) 74–85.
- [6] N. Bruckner, K. Obesser, A. Bosmann, D. Teichmann, W. Arlt, J. Dungs, P. Wasserscheid, Evaluation of industrially applied heat-transfer fluids as liquid organic hydrogen carrier systems, *ChemSuschem* 7 (2014) 229–235.
- [7] M. Niermann, S. Drünert, M. Kaltschmitt, K. Bonhoff, Liquid organic hydrogen carriers (LOHCs) – techno-economic analysis of LOHCs in a defined process chain, *Energy Environ. Sci.* 12 (2019) 290–307.
- [8] D. Teichmann, W. Arlt, P. Wasserscheid, Liquid organic hydrogen carriers as an efficient vector for the transport and storage of renewable energy, *Int. J. Hydrog. Energy* 37 (2012) 18118–18132.
- [9] H.-L. Ye, S.-X. Liu, C. Zhang, Y.-Q. Cai, Y.-F. Shi, Dehydrogenation of methylcyclohexane over Pt-based catalysts supported on functional granular activated carbon, *RSC Adv.* 11 (2021) 29287–29297.
- [10] M. Yang, Y. Dong, S. Fei, H. Ke, H. Cheng, A comparative study of catalytic dehydrogenation of perhydro-N-ethylcarbazole over noble metal catalysts, *Int. J. Hydrog. Energy* 39 (2014) 18976–18983.
- [11] B. Wang, T.-Y. Chang, Z. Jiang, J.-J. Wei, Y.-H. Zhang, S. Yang, T. Fang, Catalytic dehydrogenation study of dodecahydro-N-ethylcarbazole by noble metal supported on reduced graphene oxide, *Int. J. Hydrog. Energy* 43 (2018) 7317–7325.
- [12] F. Sotoodeh, K.J. Smith, Structure sensitivity of dodecahydro-N-ethylcarbazole dehydrogenation over Pd catalysts, *J. Catal.* 279 (2011) 36–47.
- [13] B. Wang, Y.T. Chen, T.Y. Chang, Z. Jiang, Z.Q. Huang, S.Y. Wang, C.R. Chang, Y. S. Chen, J.J. Wei, S. Yang, T. Fang, Facet-dependent catalytic activities of Pd/rGO: Exploring dehydrogenation mechanism of dodecahydro-N-ethylcarbazole, *Appl. Catal. B-Environ.* (2020) 266.
- [14] X. Chen, G. Li, M. Gao, Y. Dong, M. Yang, H. Cheng, Wet-impregnated bimetallic Pd-Ni catalysts with enhanced activity for dehydrogenation of perhydro-N-propylcarbazole, *Int. J. Hydrog. Energy* 45 (2020) 32168–32178.
- [15] C.H. Ding, T. Zhu, F.Y. Wang, Z.M. Zhang, Y. Dong, M. Yang, G.E. Cheng, H.Z. Ke, H.S. Cheng, High active Pd@mil-101 catalyst for dehydrogenation of liquid organic hydrogen carrier, *Int. J. Hydrog. Energy* 45 (2020) 16144–16152.
- [16] C.Y. Dong, Z.R. Gao, Y.L. Li, M. Peng, M. Wang, Y. Xu, C.Y. Li, M. Xu, Y.C. Deng, X. T. Qin, F. Huang, X.Y. Wei, Y.G. Wang, H.Y. Liu, W. Zhou, D. Ma, Fully exposed palladium cluster catalysts enable hydrogen production from nitrogen heterocycles, *Nat. Catal.* 5 (2022) 485–493.
- [17] X. Chen, X. Qin, Y. Jiao, M. Peng, J. Diao, P. Ren, C. Li, D. Xiao, X. Wen, Z. Jiang, N. Wang, X. Cai, H. Liu, D. Ma, Structure-dependence and metal-dependence on atomically dispersed Ir catalysts for efficient n-butane dehydrogenation, *Nat. Commun.* 14 (2023) 2588.
- [18] X. Chen, M. Peng, X. Cai, Y. Chen, Z. Jia, Y. Deng, B. Mei, Z. Jiang, D. Xiao, X. Wen, N. Wang, H. Liu, D. Ma, Regulating coordination number in atomically dispersed Pt species on defect-rich graphene for n-butane dehydrogenation reaction, *Nat. Commun.* 12 (2021) 2664.
- [19] Z. Feng, X. Chen, X. Bai, Catalytic dehydrogenation of liquid organic hydrogen carrier dodecahydro-N-ethylcarbazole over palladium catalysts supported on different supports, *Environ. Sci. Pollut. Res. Int.* 27 (2020) 36172–36185.
- [20] Z.W. Chen, M.D. Zhang, J.W. Hua, M. Yang, Y. Dong, H.S. Cheng, Remarkable activity of Pd catalyst supported on alumina synthesized via a hydrothermal route for hydrogen release of perhydro-N-propylcarbazole, *Int. J. Hydrog. Energy* 46 (2021) 9718–9729.
- [21] D.D. Wang, W.B. Gong, J.F. Zhang, M.M. Han, C. Chen, Y.X. Zhang, G.Z. Wang, H. M. Zhang, H.J. Zhao, Encapsulated Ni-Co alloy nanoparticles as efficient catalyst for hydrodeoxygenation of biomass derivatives in water, *Chin. J. Catal.* 42 (2021) 2027–2037.
- [22] G.G. Yang, J.W. Zhu, P.F. Yuan, Y.F. Hu, G. Qu, B.A. Lu, X.Y. Xue, H.B. Yin, W. Z. Cheng, J.Q. Cheng, W.J. Xu, J. Li, J.S. Hu, S.C. Mu, J.N. Zhang, Regulating Fe-spin state by atomically dispersed Mn-N in Fe-N-C catalysts with high oxygen reduction activity, *Nat. Commun.* 12 (2021) 1734–1743.

- [23] K.N. Wood, R. O'Hayre, S. Pylypenko, Recent progress on nitrogen/carbon structures designed for use in energy and sustainability applications, *Energy Environ. Sci.* 7 (2014) 1212–1249.
- [24] Q.X. Lai, J. Zheng, Z.M. Tang, D. Bi, J.X. Zhao, Y.Y. Liang, Optimal configuration of N-Doped carbon defects in 2D turbostratic carbon nanomesh for advanced oxygen reduction electrocatalysis, *Angew. Chem. Int. Ed.* 59 (2020) 11999–12006.
- [25] Z. Dong, G.L. Liu, S.C. Zhou, Y.Y. Zhang, W.L. Zhang, A.X. Fan, X. Zhang, X.P. Dai, Restructured Fe-Mn Alloys encapsulated by N-doped carbon nanotube catalysts derived from bimetallic MOF for enhanced oxygen reduction reaction, *ChemCatChem* 10 (2018) 5475–5486.
- [26] Z.Z. Wei, Y.Q. Chen, J. Wang, D.F. Su, M.H. Tang, S.J. Mao, Y. Wang, Cobalt encapsulated in N-doped graphene layers: an efficient and stable catalyst for hydrogenation of quinoline compounds, *ACS Catal.* 6 (2016) 5816–5822.
- [27] B. Sahoo, C. Kreyenschulte, G. Agostini, H. Lund, S. Bachmann, M. Scalone, K. Junge, M. Beller, A robust iron catalyst for the selective hydrogenation of substituted (iso)quinolones, *Chem. Sci.* 9 (2018) 8134–8141.
- [28] H.T. Hu, Y.Q. Nie, Y.W. Tao, W.Y. Huang, L. Qi, R.F. Nie, Metal-free carbocatalyst for room temperature acceptorless dehydrogenation of N-heterocycles, *Sci. Adv.* 8 (2022) 9478–9487.
- [29] B.W. Zhong, R. Huang, D.S. Su, H.Y. Liu, Effect of graphitization of oxygen-modified carbon nanotubes in selective oxidation of acrolein, *Catal. Today* 330 (2019) 142–148.
- [30] M.M. Rahman, M. Muttakin, A. Pal, A. Shafiqullah, B.B. Saha, A statistical approach to determine optimal models for IUPAC-classified adsorption isotherms, *Energies* 12 (2019) 4565–4598.
- [31] X. Li, H. Su, G. Ren, S. Wang, A highly stable Pd/SiO₂/cordierite monolith catalyst for 2-ethyl-anthraquinone hydrogenation, *RSC Adv.* 5 (2015) 100968–100977.
- [32] C.X. Han, W.W. Yi, Z.P. Li, C. Dong, H.Z. Zhao, M. Liu, Single-atom palladium anchored N-doped carbon enhanced electrochemical detection of furazolidone, *Electrochim. Acta* 447 (2023) 142083–142092.
- [33] S.Z. Hu, X.S. Zhang, S.J. Gao, G.M. Luo, S.G. Sun, 2,2'-bipyridine palladium (II) complexes derived N-doped carbon encapsulated palladium nanoparticles for formic acid oxidation, *Electrochim. Acta* 413 (2022) 140179–140687.
- [34] C.A. Teles, P.M. de Souza, A.H. Braga, R.C. Rabelo-Neto, A. Teran, G. Jacobs, D. E. Resasco, F.B. Noronha, The role of defect sites and oxophilicity of the support on the phenol hydrodeoxygenation reaction, *Appl. Catal. B-Environ.* 249 (2019) 292–305.
- [35] C. Li, Q. Zhang, Z. Xu, L. Liu, T. Zhu, Z. Chen, Y. Dong, M. Yang, Ce-promoted highly active bifunctional Pd/Al₂O₃ catalyst for reversible catalytic hydrogenation and dehydrogenation of N-propylcarbazole, *Int. J. Hydrog. Energ.* 48 (2023) 90–100.
- [36] S.F. Parker, H.C. Walker, S.K. Callear, E. Grunewald, T. Petzold, D. Wolf, K. Mobus, J. Adam, S.D. Wieland, M. Jimenez-Ruiz, P.W. Albers, The effect of particle size, morphology and support on the formation of palladium hydride in commercial catalysts, *Chem. Sci.* 10 (2019) 480–489.
- [37] S. Liu, X. Chen, Z.-J. Wu, X.-C. Zheng, Z.-K. Peng, P. Liu, Chitosan-reduced graphene oxide hybrids encapsulated Pd(0) nanocatalysts for H₂ generation from ammonia borane, *Int. J. Hydrog. Energ.* 44 (2019) 23610–23619.
- [38] Z.C. Mao, L.H. Liu, H.B. Yang, Y.L. Zhang, Z.Q. Yao, H. Wu, Y.Q. Huang, Y.H. Xu, B. Liu, Atomically dispersed Pd electrocatalyst for efficient aqueous phase dechlorination reaction, *Electrochim. Acta* 391 (2021) 138886–138893.
- [39] Z. Chen, M. Zhang, J. Hua, M. Yang, Y. Dong, H. Cheng, Remarkable activity of Pd catalyst supported on alumina synthesized via a hydrothermal route for hydrogen release of perhydro-N-propylcarbazole, *Int. J. Hydrog. Energ.* 46 (2021) 9718–9729.
- [40] L.L. Ling, W.J. Yang, P. Yan, M. Wang, H.L. Jiang, Light-assisted CO₂ hydrogenation over Pd₃Cu@UiO-66 promoted by active sites in close proximity, *Angew. Chem. -Int. Ed.* 61 (2022) 6396–6402.
- [41] W. Zhang, H.Z. Wang, J.W. Jiang, Z.J. Sui, Y.A. Zhu, D. Chen, X.G. Zhou, Size dependence of Pt catalysts for propane dehydrogenation: from atomically dispersed to nanoparticles, *ACS Catal.* 10 (2020) 12932–12942.
- [42] H. Meng, Y.S. Yang, T.Y. Shen, Z.M. Yin, J. Zhang, H. Yan, M. Wei, Highly efficient hydrogen production from dehydrogenation reaction of nitrogen heterocycles via Pd⁰-Pd^δ+synergistic catalysis, *ACS Catal.* 13 (2023) 9234–9244.
- [43] K.X. Ma, W.Q. Liao, W. Shi, F.K. Xu, Y. Zhou, C. Tang, J.Q. Lu, W.J. Shen, Z. H. Zhang, Ceria-supported Pd catalysts with different size regimes ranging from single atoms to nanoparticles for the oxidation of CO, *J. Catal.* 407 (2022) 104–114.
- [44] X. Zhang, Q. Gu, Y. Ma, Q. Guan, R. Jin, H. Wang, B. Yang, J. Lu, Support-Induced unusual size dependence of Pd catalysts in chemoselective hydrogenation of para-chloronitrobenzene, *J. Catal.* 400 (2021) 173–183.
- [45] S. Panic, A. Kukovec, G. Boskovic, Design of catalytic carbon nanotube-based reactor for water denitration - The impact of active metal confinement, *Appl. Catal. B-Environ.* 225 (2018) 207–217.
- [46] X.L. Pan, X.H. Bao, The effects of confinement inside carbon nanotubes on catalysis, *Acc. Chem. Res.* 44 (2011) 553–562.
- [47] Y. Dong, M. Yang, P. Mei, C.G. Li, L.L. Li, Dehydrogenation kinetics study of perhydro-N-ethylcarbazole over a supported Pd catalyst for hydrogen storage application, *Int. J. Hydrog. Energ.* 41 (2016) 8498–8505.
- [48] X.D. Chen, G. Li, M. Gao, Y. Dong, M. Yang, H.S. Cheng, Wet-impregnated bimetallic Pd-Ni catalysts with enhanced activity for dehydrogenation of perhydro-N-propylcarbazole, *Int. J. Hydrog. Energ.* 45 (2020) 32168–32178.
- [49] Y. Dong, M. Yang, T. Zhu, X. Chen, G. Cheng, H. Ke, H. Cheng, Fast dehydrogenation kinetics of perhydro-N-propylcarbazole over a supported Pd catalyst, *ACS Appl. Energy Mater.* 1 (2018) 4285–4292.
- [50] C. Ding, T. Zhu, F. Wang, Z. Zhang, Y. Dong, M. Yang, G. Cheng, H. Ke, H. Cheng, High active Pd@mil-101 catalyst for dehydrogenation of liquid organic hydrogen carrier, *Int. J. Hydrog. Energ.* 45 (2020) 16144–16152.
- [51] Z. Feng, X. Bai, 3D-mesoporous KIT-6 supported highly dispersed Pd nanocatalyst for dodecahydro-N-ethylcarbazole dehydrogenation, *Microporous Mesoporous Mater.* 335 (2022) 111789–111800.
- [52] Z. Jiang, S. Guo, T. Fang, Enhancing the catalytic activity and selectivity of PdAu/SiO₂ bimetallic catalysts for dodecahydro-N-ethylcarbazole dehydrogenation by controlling the particle size and dispersion, *ACS Appl. Energy Mater.* 2 (2019) 7233–7243.
- [53] X. Li, F. Wu, W. Zhou, C. Chen, J. Wang, B. Li, H. Chen, J. Fu, Low-temperature dehydrogenation of dodecahydro-N-ethylcarbazole catalyzed by PdCo bimetallic oxide, *Chem. Eng. Sci.* 273 (2023) 118650–118659.
- [54] B. Wang, T. Yan, T. Chang, J. Wei, Q. Zhou, S. Yang, T. Fang, Palladium supported on reduced graphene oxide as a high-performance catalyst for the dehydrogenation of dodecahydro-N-ethylcarbazole, *Carbon* 122 (2017) 9–18.
- [55] Z. Jiang, X. Gong, B. Wang, Z. Wu, T. Fang, A experimental study on the dehydrogenation performance of dodecahydro-N-ethylcarbazole on M/TiO₂ catalysts, *Int. J. Hydrog. Energ.* 44 (2019) 2951–2959.
- [56] B. Hammer, J.K. Nørskov, Theoretical surface science and catalysis-calculations and concepts. *Advances in Catalysis*, Academic Press, 2000, pp. 71–129.